Chapter 18

III-V Multi-Junction Solar Cells

Gui jiang Lin, Jingfeng Bi, Minghui Song,
Jianqing Liu, Weiping Xiong and Meichun Huang

Additional information is available at the end of the chapter

http://dx.doi.org/10.5772/50965

1. Introduction

Photovoltaic is accepted as a promising technology that directly takes advantage of our planet's ultimate source of power, the sun. When exposed to light, solar cells are capable of producing electricity without any harmful effect to the environment or devices. Therefore, they can generate power for many years (at least 20 years) while requiring only minimal maintenance and operational costs. Currently the wide-spread use of photovoltaic over other energy sources is impeded by the relatively high cost and low efficiency of solar cells [1].

III-V multi-junction solar cells, as a new technology, offer extremely high efficiencies compared with traditional solar cells made of a single layer of semiconductor material [2]. The strong demand for higher efficiency photovoltaic has recently attracted considerable interest in multi-junction solar cells based on III-V semiconductors [3]. Depending on a particular technology, multi-junction solar cells are capable of generating approximately twice as much power under the same conditions as traditional solar cells made of silicon. Unfortunately, multi-junction solar cells are very expensive, so they are mainly used in high performance applications such as satellites at present. However, in our opinion, with the concentrator technology, the tandem cell will play a role in the future energy market. The state-of-the-art high efficiency III-V solar cells utilize a triple junction structure which consists of the Ge bottom sub-cell (0.67 eV) formed on the Ge substrate homogeneously, the $Ga_{0.99}In_{0.01}As$ middle sub-cell (1.36 eV), and the lattice matched (LM) $Ga_{0.5}In_{0.5}P$ top sub-cell (1.86 eV) [4,5]. It has reached conversion efficiencies up to 40% at concentrations of hundreds of suns under the AM1.5D low aerosol optical depth (AOD) spectrum [4]. The GaInP/GaInAs/Ge triple-junction cells have also been demonstrated with efficiencies up to 30% under one-sun AM0 spectrum for space applications. Multi-junction solar cells based on III-V materials have achieved the highest efficiencies of any present photovoltaic devices. Addi-

tionally, these devices are the only solar cells currently available with efficiencies above 30%. The high efficiency is due to the reduction of thermalization and transmission losses in solar cells when the number of p-n junctions is increased.

Future terrestrial cells will likely feature four or more junctions with a performance potential capable of reaching over 45% efficiency at concentration of hundreds of suns. The 4-, 5-, or 6-junction solar cells with concentrator trade lower current densities for higher voltage and divide the solar spectrum more efficiently. The lower current densities in these cells can significantly reduce the resistive power loss (I^2R) at high concentrations of suns when compared with the 3-junction cell [6].

High-efficiency GaInP/GaAs/InGaAs triple-junction solar cells grown inversely with a metamorphic bottom junction could be achieved by replacing the bottom Ge sub-cell with 1 eV energy gap material. $In_{0.3}Ga_{0.7}As$ is the promised candidate, if without the lattices mis-match (LMM, around 2%) with the other two sub-cells. Therefore, the LM top and middle sub-cells were grown first, and the graded buffers were employed between middle and bottom cells to overcome the mismatch and to prevent the threading dislocations. The substrate was removed for the reusing. This inverted metamorphic, monolithic triple junction solar cells could be obtained with at least 2% higher efficiency than the traditional one theoretically [7].

A metamorphic $Ga_{0.35}In_{0.65}P/Ga_{0.83}In_{0.17}As$/Ge triple-junction solar cell is studied to provide current-matching of all three sub-cells and thus give a device structure with virtually ideal energy gap combination. It is demonstrated that the key for the realization of this device is the improvement of material quality of the lattice-mismatched layers as well as the development of a highly relaxed $Ga_{1-y}In_yAs$ buffer structure between the Ge substrate and the middle cell. This allows the metamorphic growth with low dislocation densities below 10^6 cm^{-2}. The performance of the device has been demonstrated by a conversion efficiency of 41.1% at 454 suns AM1.5D [8].

In this chapter, the theoretical and experimental investigation of the most sophisticated, industrialized and commercialized GaInP/GaInAs/Ge triple junction solar cell was extensively described. Accelerated aging tests of the high concentration multi-junction solar cells and discussions on outdoor power plant performances were also presented.

2. Theoretical study on optimization of high efficiency multi-junction solar cells

In designing GaInP/GaInAs/Ge triple-junction cells, the principles for maximising cell efficiency are: (1) increasing the amount of light collected by each cell that is turned into carriers, (2) increasing the collection of light-generated carriers by each p-n junction, (3) minimising the forward bias dark current, and (4) photocurrents matching among sub-cells.

In practice, basic designs for these solar cells involve various doping concentrations and layer thicknesses for the window, emitter, base, and back surface field (BSF) regions in each sub-cell. In order to optimize the designs, a rigorous model including optical and electrical

http://dx.doi.org/10.5772/50965

modules was developed to analyse the bulk parameters effect on the external quantum efficiency, photocurrent and photovoltage of the GaInP/GaInAs/Ge multi-junction solar cells.

2.1. Theoretical approach

We present here a brief description of the equations used in our model. Thorough treatments of photovoltaic devices can be found elsewhere [9]. A schematic of a typical lattice-matched GaInP/GaInAs/Ge solar cell is shown in Figure1. It consists of an n/p GaInP junction on top of an n/p GaInAs junction which lies on an n/p Ge junction. The triple junction cells are series connected by two p++/n++ tunnel junctions.

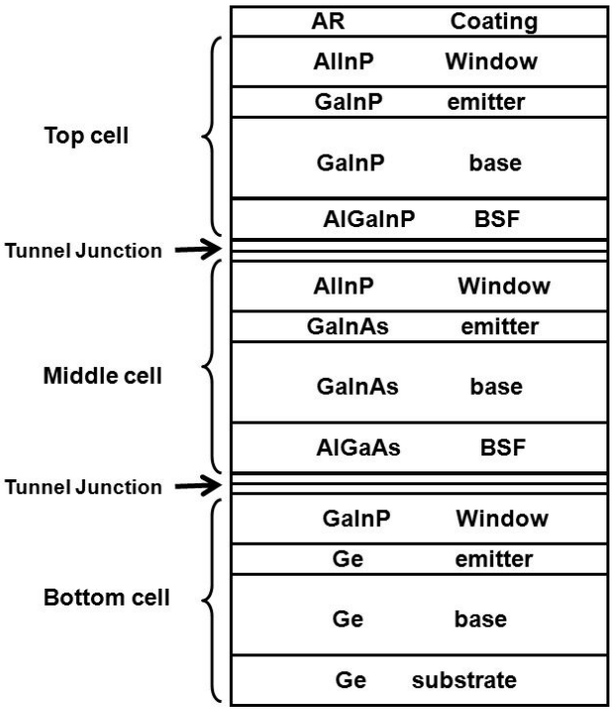

Figure 1. Solar cell structure used for simulation.

The solar spectrum, striking the front of the cell, includes ultraviolet, visible, and infrared lights. The absorption coefficient for short-wavelength light is quite large, and most of the blue light is absorbed very close to the front of the cell for generating photo carriers. Light with energy slightly larger than the energy gap is weakly absorbed throughout the cell. Light with energy less than the energy gap passes through the front cell and is absorbed in the next one. The photo carriers generated by the short-wavelength light diffuse inside the cell until they are either collected at the p-n junction or recombined with a majority carrier in bulk or at interface. The efficiency of the solar cell increase when all the photo carriers are collected at the junction instead of recombining elsewhere. Thus, recombination is at the front and back of the cell effects on the efficiency of the cell.

At the first level approximation, multi-junction cells behave like homo-junction cells in series, so their open circuit voltage is the summation of the voltages of the sub-cells, while their

short circuit current is that of the sub-cell with the smallest current. Hence, the performance of a multi-junction cell can be obtained from the performance of each sub-cell, evaluated independently. The load current density J is represented by the superposition of two diode currents and the photo-generated current,

$$J = J_{ph} - J_{01}(e^{qV/kT} - 1) - J_{02}(e^{qV/2kT} - 1) \tag{1}$$

Where J_{ph} is the photocurrent density, J_{01} the ideal dark saturation current component and J_{02} the space charge non-ideal dark saturation current component.

The photocurrent density and dark current density are given by the sum of the photocurrents and the sum of the dark current density, respectively, generated in the emitter, the base and the depleted region of the cell. [9] We have

$$J_{ph} = J_{emitter} + J_{base} + J_{depleted} \tag{2}$$

$$J_{emitter} = \frac{qF(1-R)\alpha L_p}{(\alpha L_p)^2 - 1} \left\{ \frac{\frac{S_p L_p}{D_p} + \alpha L_p - e^{-\alpha(d_e - W_n)} \left(\frac{S_p L_p}{D_p} \cosh[(d_e - W_n)/L_p] + \sinh[(d_e - W_n)/L_p] \right)}{\frac{S_p L_p}{D_p} \sinh[(d_e - W_n)/L_p] + \cosh[(d_e - W_n)/L_p]} \right\} - \alpha L_p e^{-\alpha(d_e - W_n)} \tag{3}$$

$$J_{base} = \frac{qF(1-R)\alpha L_n}{(\alpha L_n)^2 - 1} e^{-\alpha(d_b - W_n + W)} \left\{ \alpha L_n - \frac{\frac{S_n L_n}{D_n} \left(\cosh[(d_e - W_n)/L_n] - e^{-\alpha(d_b - W_p)} \right) + \sinh[(d_b - W_p)/L_n] + \alpha L_n e^{-\alpha(d_b - W_p)}}{\frac{S_n L_n}{D_n} \sinh[(d_b - W_p)/L_n] + \cosh[(d_b - W_p)/L_n]} \right\} \tag{4}$$

$$J_{depleted} = qF(1-R)e^{-\alpha(d_e - W_n)}(1 - e^{-\alpha W}) \tag{5}$$

$$J_{01} = J_{01,emitter} + J_{01,base} \tag{6}$$

http://dx.doi.org/10.5772/50965

$$J_{01,emitter} = q\frac{n_i^2}{N_D}\frac{D_p}{L_p}\left\{\frac{S_pL_p/D_p\cosh[(d_e-W_n)/L_p]+\sinh[(d_e-W_n)/L_p]}{S_pL_p/D_p\sinh[(d_e-W_n)/L_p]+\cosh[(d_e-W_n)/L_p]}\right\} \quad (7)$$

$$J_{01,base} = q\frac{n_i^2}{N_A}\frac{D_n}{L_n}\left\{\frac{S_nL_n/D_n\cosh[(d_b-W_p)/L_n]+\sinh[(d_b-W_p)/L_n]}{S_nL_n/D_n\sinh[(d_b-W_p)/L_n]+\cosh[(d_b-W_p)/L_n]}\right\} \quad (8)$$

$$J_{02} = \frac{Wn_i}{2(V_d-V)\tau} \quad (9)$$

Where q is electron charge, F the incident photon flux, α is an optical absorption coefficient and R is the reflectance of the anti-reflective coating. n_i is the intrinsic carrier concentration, N_A and N_D are the concentrations of acceptors and donors. d_e is the emitter thickness, d_b the base thickness, L_p the hole diffusion length in the emitter, L_n the electron diffusion length in the base, S_p the hole surface recombination velocity in the emitter, S_n the electron surface recombination velocity in the base, D_p the hole diffusion coefficient in the emitter, D_n the electron diffusion coefficient in the base, and τ is the non-radiative carrier lifetime. T_F is the transmission of incident photon flux into the sub-cell under consideration.

The build-in voltage V_d of the junction, the thickness of the depleted layer in the emitter W_n , the thickness of the depleted layer in the base W_p , and the total depleted zone thickness W , are given by [10],

$$V_d = kT\log\left(\frac{N_DN_A}{n_i^2}\right) \quad (10)$$

$$W = \sqrt{2\varepsilon\frac{N_D+N_A}{N_DN_A}(V_d-V-2kT)} \quad (11)$$

$$W_n = W/(1+N_D/N_A) \quad (12)$$

$$W_p = W - W_n \quad (13)$$

Where k is the Boltzmann constant, ε the dielectric constant and T the temperature (T =25 °C was used in this paper). It is important to note that F and α depend on the wavelength, whereas D_p , D_n , L_p , L_n and τ depend on the doping concentration [11].

The optical model proposed in this paper is based on the transfer matrix formalism. It allows calculating the incident optical spectrum on each sub-cell from the solar spectrum. Each layer of the multi-junction is described by a transfer matrix M which is defined by

$$M = \begin{pmatrix} M_{0,0} M_{0,1} \\ M_{1,0} M_{1,1} \end{pmatrix} = \begin{pmatrix} \cos\left(d\dfrac{2\pi(n - i\lambda\alpha/4\pi)}{\lambda}\right) i\dfrac{\sin\left(d\dfrac{2\pi(n - i\lambda\alpha/4\pi)}{\lambda}\right)}{(n - i\lambda\alpha/4\pi)} \\ (n - i\lambda\alpha/4\pi)\sin\left(d\dfrac{2\pi(n - i\lambda\alpha/4\pi)}{\lambda}\right) \cos\left(d\dfrac{2\pi(n - i\lambda\alpha/4\pi)}{\lambda}\right) \end{pmatrix} \tag{14}$$

Where n and d are the refraction index and the thickness of the layer, respectively. The transmission coefficient T_M [12] of the layer is then given by

$$T_M = \frac{4n_0^2}{(n_0 M_{0,0} + n_0 n_s M_{0,1} + M_{1,0} + n_s M_{1,1})^2} \tag{15}$$

Where n_0 is the superstrate refraction index and n_s is the substrate refraction index of the sub-cell. The $M_{i,j}$ coefficients refer to the matrix transfer elements. Thus, it is possible to determine the incident spectrum on each sub-cell. The incident photon flux in GaInP, GaInAs and Ge sub-cells are given by

$$F_{GaInP} = T_{ARC} F_{solar} \tag{16}$$

$$F_{GaInAs} = T_{ARC} T_{GaInP} F_{solar} \tag{17}$$

$$F_{Ge} = T_{GaInAs} T_{GaInP} T_{ARC} F_{solar} \tag{18}$$

where F_{solar} is the incident photon flux, T_{ARC} , T_{GaInP} and T_{GaInAs} are the transmission coefficient of the anti-reflective coating, the GaInP sub-cell and the GaInAs sub-cell, respectively. This model includes optical and electrical modules. Thus, it allows the calculation of the quantity of photons arriving at each junction from the solar spectrum. Then, the electrical model calculates, via interface recombination velocity, the photocurrents in the space charge region, the emitter and the base for each junction.

2.2. Solar cell structures and parameters

To calculate the power production of the GaInP/GaInAs/Ge triple-junction cells for space applications, the incident photon flux F_{solar} was taken from a newly proposed reference air mass zero (AM0) spectra (ASTM E-490). The integration of ASTM E490 AM0 solar spectral irradiance has been made to conform to the value of the solar constant accepted by the space community, which is 1366.1 W/m^2. The transmission coefficient of the anti-reflective coating T_{ARC} was set to be a constant of 98%, while the transmission coefficients of the GaInP sub-cell and the GaInAs sub-cell are calculated according to Eqs.14 and 15, which have wavelength dependence.

http://dx.doi.org/10.5772/50965

Parameter	Ge	GaInAs	GaInP
D_n(cm²/s)	22.86	140.02	29.39
D_p(cm²/s)	10.71	4.02	1.03
L_n(cm)	5.3x10^{-3}	9.7x10^{-4}	6.3x10^{-4}
L_p(cm)	8.8x10^{-4}	7.3x10^{-5}	3.7x10^{-5}
τ (s)	8.9x10^{-7}	8.9x10^{-9}	4.2x10^{-9}

Table 1. Material parameters used for calculation in this paper.

As shown in Figure 1, typical two-terminal triple-junction cells for space application with a Ge bottom cell, a GaInAs middle cell and a GaInP top cell with energy gaps of 0.661, 1.405 and 1.85 eV, respectively. The Ge cell is built on the p-type initial substrate; therefore, the Ge base is about 150 micrometers thick, with doping concentration of about 6x10^{17} cm^{-3}; the Ge emitter is about 0.3 micrometers thick, with an n-type doping concentration of about 1x10^{19} cm^{-3}. The emitters for the other two cells are 0.1 micrometers thick with doping concentration of about 1x10^{18} cm^{-3}. Since the AM0 spectrum contains relatively more high-energy photons with energy greater than the GaInP top cell's energy gap, triple-junction cell with a very thick top cell will generally be photocurrent limited by the middle (GaInAs) cell. Therefore, the middle cell thickness was set to be thick enough (3.6 micrometers in this paper) with the doping concentration of about 2x10^{17} cm^{-3}, and the optimal top cell thickness was suggested to be about 0.52 micrometers with doping concentration of about 1x10^{17} cm^{-3}.

The absorption coefficient of the GaInP can be fitted by

$$\alpha_{GaInP} = 5.5\sqrt{(E - E_g)} + 1.5\sqrt{(E - E_g - 1)} \tag{19}$$

The absorption coefficient of the GaInAs (with In content of about 0.01) can be fitted by

$$\alpha_{GaInAs} = 3.3\sqrt{(E - E_g)} \tag{20}$$

The direct gap absorption spectra of the bulk Ge was used for calculation

$$\alpha_{Ge} = 1.9\sqrt{(E - E_g^{\Gamma})} \Big/ E \tag{21}$$

Where E is the photon energy and E_g the fundamental energy gap, both in eV, and α ▪ in 1/micrometers.

The diffusion length, the diffusion coefficient and the nonradiative carrier lifetime are calculated as a function of the doping concentration. The material parameters used for calculation are summarized in table 1.

2.3. The effect of the interface recombination on the performance of GaInP/GaInAs/Ge tandem solar cell

To have an analytical analysis, recombination velocity at only one interface among six interfaces is assumed to have a non-zero value, which is $1x10^6$ cm/s. Figure2~4 shows the total external quantum efficiencies η and the integrated photocurrent density J_{ph} of the three sub-cells, calculated from Eqs. 2-5 with the constant parameters in table 1 and with varying values of S_p and S_n . The external quantum efficiency η , defined as the probability of collecting a photo carrier for each photon, is a function of wavelength, λ, because of the λ-dependence of the absorption coefficient, α. The photocurrent density J_{ph} is obtained from the integral of the product of the η with the spectrum of interest. For large absorption coefficients, a high S_p causes dramatic decrease in the blue response as shown in Figure 2 (a), Figure 3 (a) and Figure 4 (a).

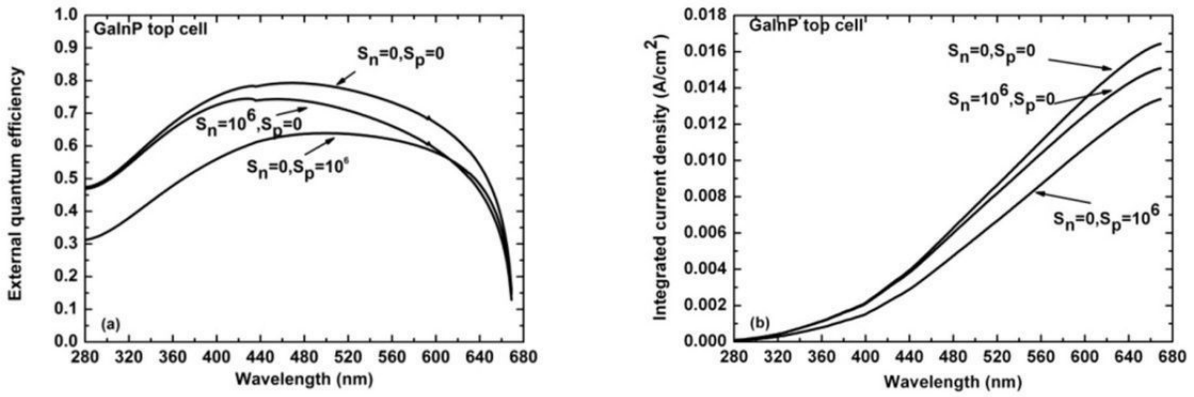

Figure 2. a) External quantum efficiency, and (b) integrated photocurrent density of the top GaInP cell for various interface recombination velocities.

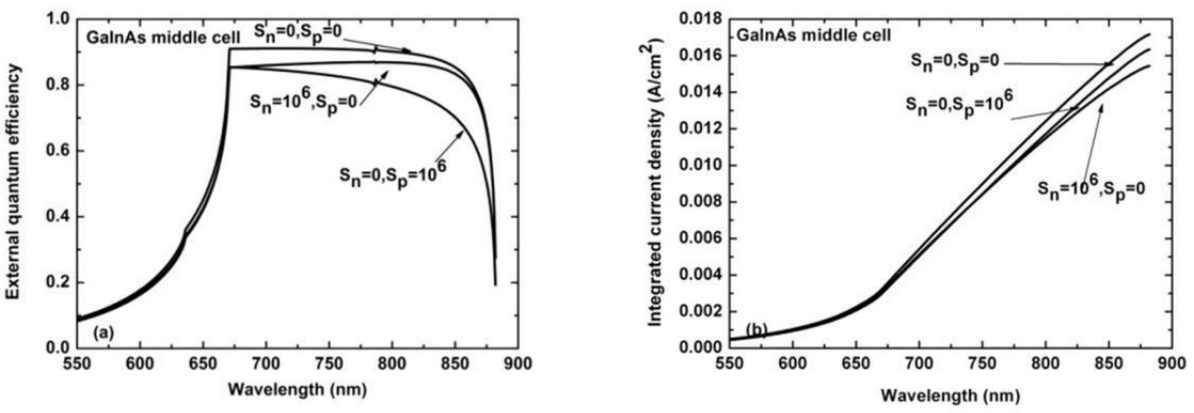

Figure 3. a) External quantum efficiency, and (b) integrated photocurrent density of the middle GaInAs cell for various interface recombination velocities.

http://dx.doi.org/10.5772/50965

However, a high S_p also causes a reduction in the red response. In contrast, high S_n causes a reduction only in the red response (Figure 2 (a), Figure 3(a)), with almost no measurable effect in the blue response for a thick cell as shown in Figure 4 (a).

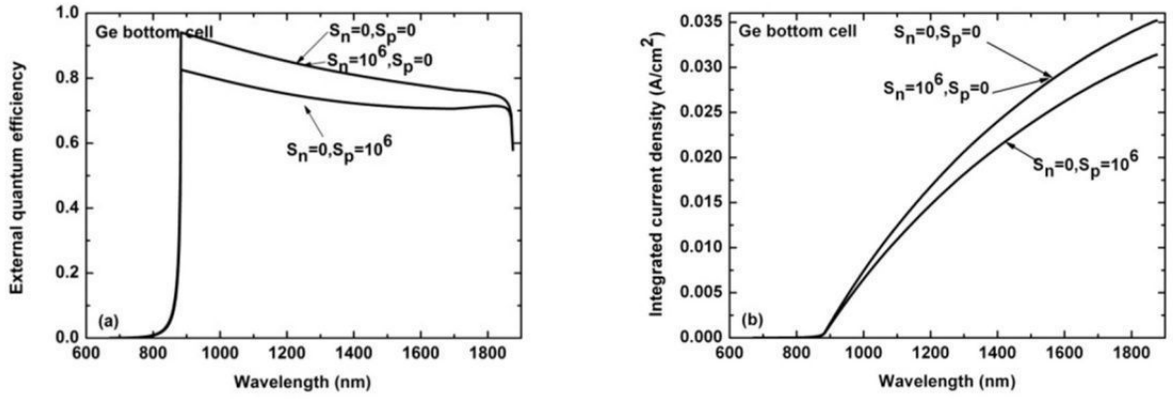

Figure 4. a) External quantum efficiency, and (b) integrated photocurrent density of the middle GaInAs cell for various interface recombination velocities.

Once the photocurrents of the three sub-cells are calculated, the short circuit current of the tandem cell is set to be the smallest of these three photocurrents. The open-circuit voltage is set to be the voltage at which the magnitude of the dark currents equals the photocurrents. The corresponding I-V characteristics of the tandem cell are plotted in Figure 5. Among all the interfaces, recombination at the top cell emitter surface is most detrimental due to the considerable drop of the cell short circuit current and to a less extent to the associated reduction in the cell voltage. While recombination effect at back interface of the bottom cell can be almost negligible because the base layer of the cell is thick enough.

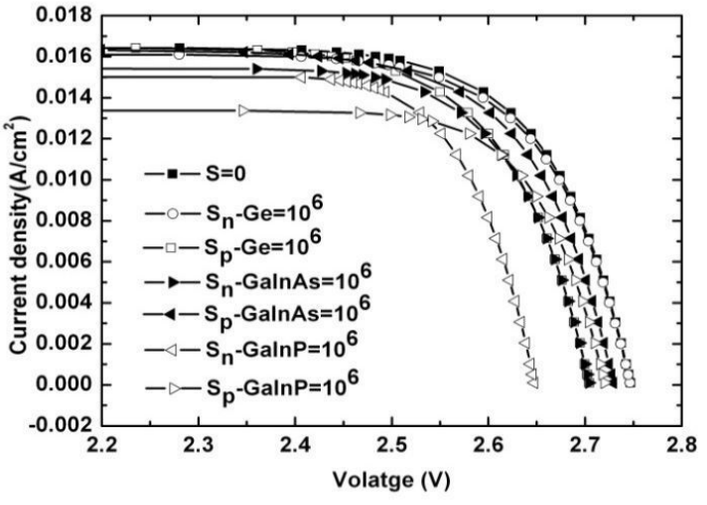

Figure 5. I-V characteristics of the GaInP/ GaInAs/ Ge tandem cell under AM0 with a recombination velocity at the indicated interface and zero elsewhere.

2.4. Optimization of high efficiency GaInP/GaInAs/Ge multi-junction solar cells

Lattice-matched GaInP/GaInAs/Ge triple-junction cells under investigation include a Ge bottom cell, a GaInAs middle cell and a GaInP top cell with energy gaps of 0.661, 1.405 and 1.85 eV, respectively. The Ge cell is built on the p-type initial substrate; the Ge base is 150 micrometers thick with doping concentration of $6x10^{17}$ cm^{-3}, and the Ge emitter is 300 nm thick with an n-type doping concentration of $1x10^{19}$ cm^{-3}. The middle cell's base is set to be thick enough (3.6 micrometers in this paper) with doping concentration of $2x10^{17}$ cm^{-3}, and its emitter is 100 nm thick with doping concentration of $1x10^{18}$ cm^{-3}. The incident photon flux is taken from a newly proposed reference air mass zero (AM0) spectra (ASTM E-490). The anti-reflective coating used in simulation includes a 30 nm AlInP top window layer; ARC composed of 52 nm ZnS and 90 nm MgF2.

It is at first assumed that recombination velocity for a top cell back surface is $1.3x10^5$ cm/s, a middle cell back surface 105 cm/s and a top cell emitter surface $5.15x10^4$ cm/s, while recombination velocities at the other three interfaces are zero. Then, the optimal top cell thickness and dopant profiles were obtained to meet high efficiency.

top cell base thickness d-base (nm)	open-circuit voltage Voc (V)	short-circuit current Jsc (A/cm^2)	fill factor	tandem cell efficiency
d-base=400 nm	2.6660	0.01720	90.56%	30.40%
d-base=450 nm	2.6664	0.01768	89.82%	30.99%
d-base=500 nm	2.6667	0.01812	88.40%	31.27%
d-base=55 0nm	2.6669	0.01777	89.82%	31.05%

Table 2. Figure-of-merits of the tandem cell for various top cell base thickness.

top cell base doping concentration (1/cm3)	open-circuit voltage Voc (V)	short-circuit current Jsc (A/cm^2)	fill factor	tandem cell efficiency
NA-base =1x1016	2.6095	0.01816	88.62%	30.74%
NA-base =5x1016	2.6503	0.01814	89.15%	31.32%
NA-base =1x1017	2.6667	0.01812	88.40%	31.27%
NA-base =5x1017	2.6981	0.01796	88.24%	31.19%

Table 3. Figure-of-merits of the tandem cell for various top cell base doping concentration.

Table 2 presents the Figure-of-merits of the tandem cell for various top cell base thicknesses with doping concentration of $1x10^{17}$ cm-3, when the top cell emitter thickness is set to 100 nm with doping concentration of $1x10^{18}$ cm^{-3}. Table 3 presents the Figure-of-merits of the

http://dx.doi.org/10.5772/50965

tandem cell for various top cell bases doping concentrations with thickness of 500 nm, when the top cell emitter thickness is set to 100 nm with doping concentration of $1x10^{18}$ cm^{-3}. It is found that photocurrents strongly depend on top cell thickness, since the AM0 spectrum contains relatively more high-energy photons with energy greater than the GaInP top cell's energy gap, and photocurrents of triple-junction cells with a very thick top cell will generally be limited by the middle (GaInAs) cell. The tandem cell efficiency reaches the largest value (31.27%) with the top cell base thickness of 500 nm, because the photocurrents of the top and middle cells almost match each other. Table 3 shows that higher doping concentration at the top cell base leads to a considerable increase of the cell voltage and a less drop of cell photocurrent. It can be deduced from table 3 that doping concentration at the top cell base should be optimized between 5 $x10^{16}$ and $1x10^{17}$ cm^{-3} to obtain higher efficiency. In order to realize the values of the Figure-of-merits shown in table 2 and table 3, the external quantum efficiency of the top cell for various top cell base thicknesses and top cell base doping concentrations are presented in Figure6 (a) and Figure6 (b), respectively. It is found that the external quantum efficiency of the top cell increases with the increasing top cell base thickness (Figure6 (a)), while at short wavelengths, the efficiency increases with the increasing top cell base doping concentration, at large wavelengths, decreases (Figure6 (b)).

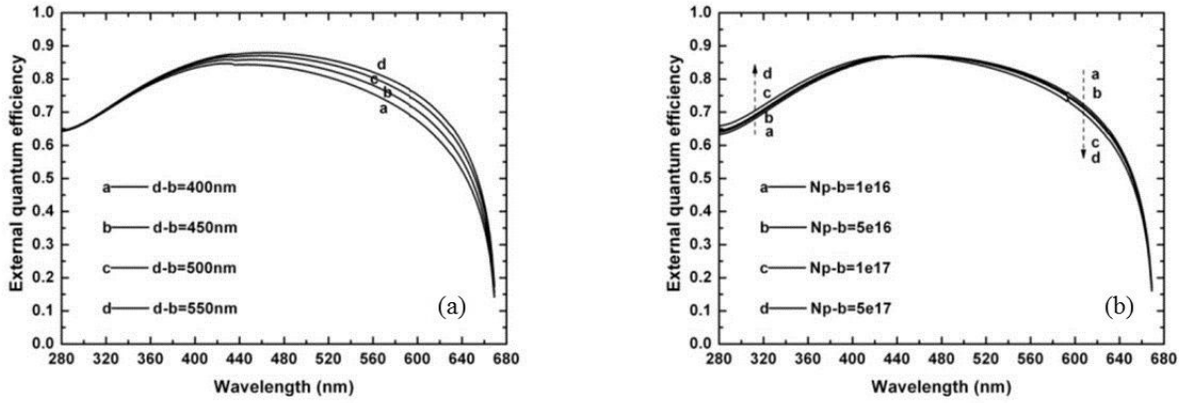

Figure 6. External quantum efficiency of the top cell for various top cell base thickness (a), and top cell base doping concentration (b).

top cell emitter thickness d-emitter (nm)	open-circuit voltage Voc (V)	short-circuit current Jsc (A/cm^2)	fill factor	tandem cell efficiency
d-emitter =50 nm	2.6680	0.01848	88.62%	31.98%
d-emitter =100 nm	2.6667	0.01812	88.40%	31.27%
d-emitter =150 nm	2.6710	0.01737	89.09%	30.25%
d-emitter =200 nm	2.6707	0.01644	89.84%	28.87%

Table 4. Figure-of-merits of the tandem cell for various top cell emitter thickness.

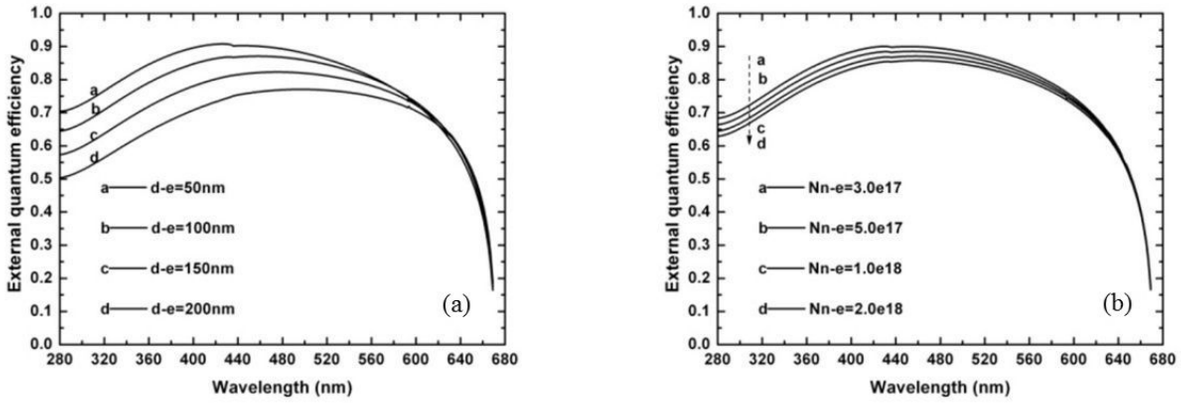

Figure 7. The external quantum efficiency of the top cell for various top cell emitter thickness (a), and top cell emitter doping concentration (b).

top cell emitter doping concentration (1/cm³)	open-circuit voltage Voc (V)	short-circuit current Jsc (A/cm²)	fill factor	tandem cell efficiency
ND -emitter =3x1017	2.6673	0.01816	89.30%	31.66%
ND -emitter =5x1017	2.6674	0.01816	88.37%	31.51%
N D-emitter =1x1018	2.6667	0.01812	88.40%	31.27%
ND -emitter =2x1018	2.6652	0.01786	88.74%	30.90%

Table 5. Figure-of-merits of the tandem cell for various top cell emitters doping concentration.

3. Experimental procedure, results and discussions

3.1. The preparation of the triple junction GaInP/GaInAs/Ge epitaxial wafers

The $Ga_{0.49}In_{0.51}P/Ga_{0.99}In_{0.01}As/Ge$ multi-junction solar cells were grown by the Veeco E475 MOCVD system on 6° off cut Germanium substrate. Standard growth conditions used were with growth pressure of 40 Torr, and rotation rate of 500 rpm. The precursors include trimethylindium (TMIn), trimethylgallium (TMGa), trimethylaluminium (TMAl), arsine, phosphine and diethyl-tellurium (DETe), diethyl-zink (DEZn). Top and middle sub-cells include the following layers: back-surface field (BSF) layer, base, emitter and window. The Ge-sub-cell consists of a base (substrate), a diffused emitter and a window. Sub-cells are connected in series by tunnel diodes, which in turn include highly doped thin (10–20 nm) layers. The growth temperature of 650 °C was applied to the layers consisting of the $Ga_{0.99}In_{0.01}As$ buffer, middle cell layers, top cell layers and GaAs cap. AlGaAs was used as to the middle and top cell BSF, and AlInP as the window layer of InGaAs middle cell and GaInP top cell.

http://dx.doi.org/10.5772/50965

The Ge sub-cell is an important part of the structure of this cell, contributing 10% or more of the total cell efficiency [13]. The Ge junction is formed during III - V /Ge interface epitaxy. Group V elements such as P and As are n-type dopants in Ge, so the emitter of Ge junction was formed by diffusion of V elements during the deposition of III - V epilayers. In addition, the structure of Ge is different from the III - V materials such as GaAs and GaInP, the connection between Ge substrate and buffer layer or initial layer is important to the growth quality on buffer layer and the performance of Ge sub-cell. In this chapter, based on plenty of experiments, GaInP is selected as a suitable buffer material to be grown between the substrate and the active region of the device. Several researches on III - V materials grown on p-doped Ge substrate have indicated that the bottom Ge cell efficiency decreases as the thickness of the emitter increases, mainly owing to the lowering of the short circuit current. For this reason, GaInP is an optimized option with smaller diffusion length than GaAs. In addition, GaInP is also an appropriate material for the window layer of Ge junction.

The electrochemical capacitance-voltage results of GaInP initial layer grown on Ge indicate that the diffusion length of P is about 200 nm, when a thin Ge emitter for excellent performance of Ge sub-cell is fabricated. In the past, GaAs was employed as the middle cell material, and the 0.08% lattice-mismatch between GaAs and Ge was thought to be negligibly. To obtain enough current matched to the top cell, the middle cell was often designed to be 3~4 micrometers thick, but misfit-dislocations were generated in thick GaAs layers and deteriorated cell performance [5]. By adding about 1% indium into the GaAs cell layers, all cell layers are lattice-matched precisely to the Ge substrate. Application of InGaAs middle cell to lattice-match Ge substrates has demonstrated to be able to increase open-circuit voltage (Voc) due to lattice-matching and short-circuit current density (Jsc) due to the decrease of the energy gap in the middle cell.

The $Ga_{0.49}In_{0.51}P/Ga_{0.99}In_{0.01}As$/Ge multi-junction solar cells for terrestrial concentrator application operate at high current densities higher than 10A/cm^2. This brings specific challenges to the tunnel diode structures that are used for the series connection of the sub-cells. So the tunnel junction (TJ) growth is one of the most important issues affecting multi-junction solar cell performance. The problems of TJ growth are related to obtaining transparent and uniformly highly doped layer without any degradation of surface morphology [14]. The thickness of each side of the TJ junction has to be in the order of tens of nanometres, while the required doping has to be around 10^{19}~10^{20} cm^{-3}. The reaching of the high doping level requires very different growth temperatures, in order to obtain an abrupt doping profile. In this experiment, the growth of tunnel junction was carried out at temperature of 600 °C which is about 50 °C lower than the growth temperature of other layers. DETe and CCl4 were used as N-type dopant and P-type dopant respectively to fabricate small thickness, high doping AlGaAs/GaAs tunnel junctions.

GaInP lattice-matched to GaAs exhibits anomalous changes in the energy gap, depending on the growth conditions and the substrate misorientation [15]. These changes are the results of the spontaneous ordering during the growth of the cation-site elements (Ga and In) in planes parallel to the (111). One of changes is a lowering of the energy gap of the material, whose exact value depends on the degree of ordering. It appears to be the 100 meV reductions. The

$Ga_{0.49}In_{0.51}P/Ga_{0.99}In_{0.01}As/Ge$ multi-junction solar cells' performance depends on the energy gap of the GaInP top cell. The theoretical calculations for this combination of materials indicate that, to achieve maximum efficiencies, the energy gap of the GaInP top cell should be about 1.89 eV. The GaInP should be completely disordered. However, the MOCVD growth conditions that produce such a material have deleterious effects on the growth quality of GaInP, which determines the performance of the solar cell. To sum up, the growth of high quality GaInP with a maximizing degree of disorder is important for super high efficiency multi-junction solar cells. To fulfil this purpose, precise controls of the growth conditions including the growth temperature, growth rate and V/III ratio were carried out in our experiments. Based on the experimental results and theoretical calculations, the growth of GaInP was carried out at 640 °C, V/III ratio about 40, and growth rates of 0.6 nm/s.

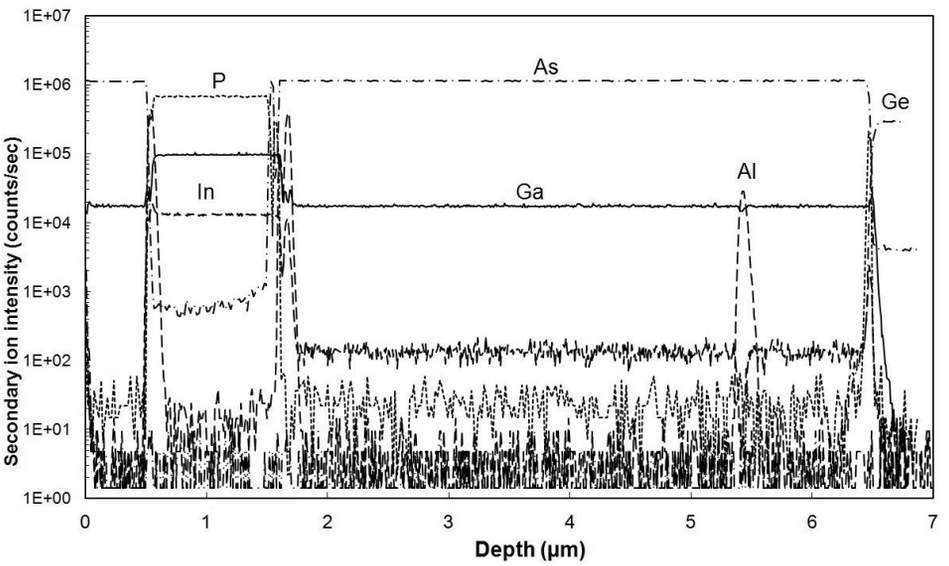

Figure 8. The SIMS spectrum of the $Ga_{0.49}In_{0.51}P/Ga_{0.99}In_{0.01}As/Ge$ multi-junction solar cells.

The SIMS spectrum of the Ga0.49In0.51P/Ga0.99In0.01As/Ge multi-junction solar cells is calibrated and shown in Figure 8. With the elemental depth profile, we can clearly identify the cell structure and the doping level and the thickness of different functional layers.

3.2. The chip processing procedure and optimization

3.2.1. The process procedure of the multi-junction solar cell

The process designed for the concentrator multi-junction solar cells is as follows: the different electrode patterns on the front and back surfaces of the GaInP/ GaInAs/Ge epitaxial wafer are formed first, and then the wafer will be separated into independent cell chips by the methods of chemical etch and/or physical wheel-cutting. Figure 9 shows photos of the GaInP/ GaInAs/Ge epitaxial wafers and chips on wafer process stage. Figure 10 shows the principal process flow. The monolithic device structures of three sub-cells are grown on the

http://dx.doi.org/10.5772/50965

Ge substrate. The graphical front electrode (negative electrode) and the non-graphical back electrode (positive electrode) will then be deposited on the both surfaces of the epitaxial wafers with a series steps of lithography, electrode deposition, metal alloy, cap layer etching, AR coating and so on.

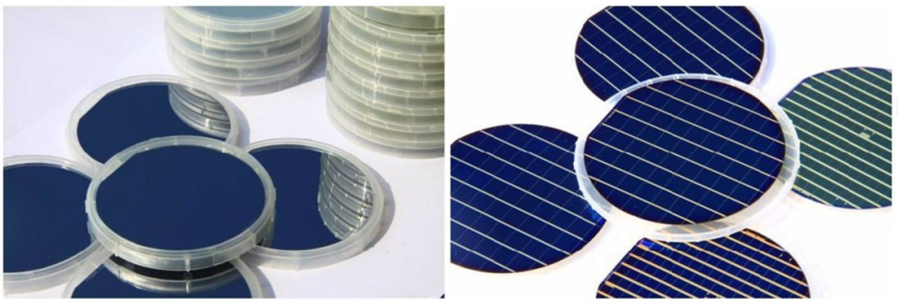

Figure 9. GaInP/ GaInAs/Ge epitaxial wafers (a), chips on wafers (b).

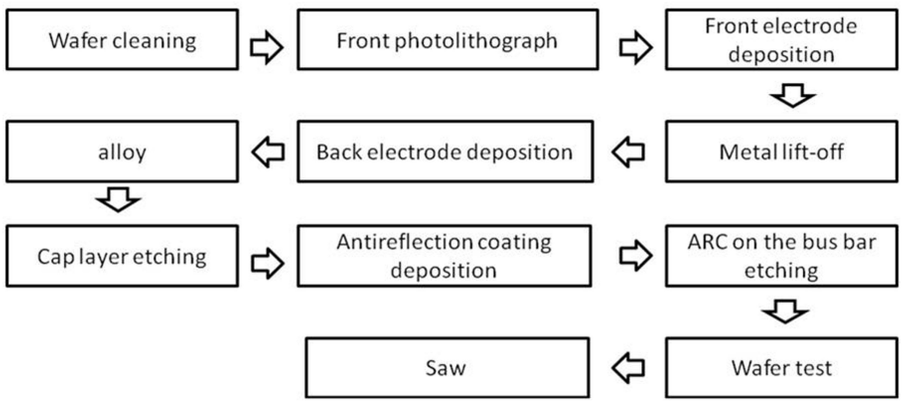

Figure 10. The principal chip process flow.

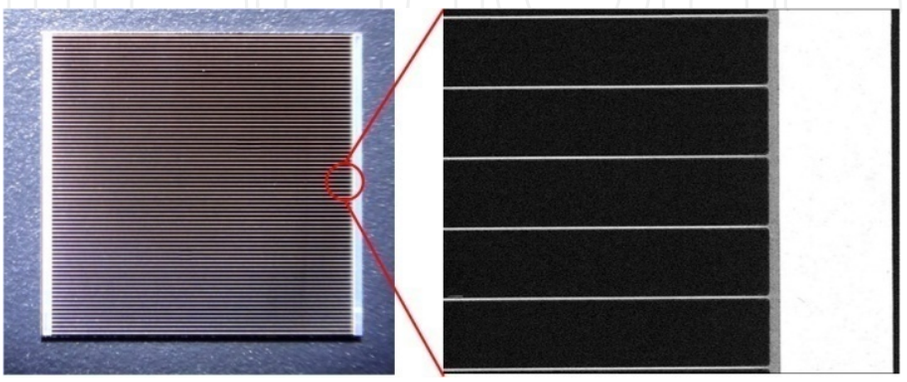

Figure 11. The detail of the graphical front electrode.

Figure11 shows the isolated solar cell and details of the front electrode. Two busbars locate at the edge of the solar cell chip with some parallel gridlines between them. The multi-layer metal structure mainly includes ohmic contact layer, adhesion or barrier layer, conductive layer, and protective layer. The ohmic contact layer will faintly diffuse to the cap layer of the epitaxial wafer after an anneal process, which can decrease the contact resistance between the electrodes and the cap layer. When the photocurrents are generated in the cells, the gridlines will collect and then transfer the currents to the busbars. Finally the golden wires bonded on the busbars will export the currents to the external circuitry.

3.2.2. Research on the process technology optimization

3.2.2.1. Grid line design

Series resistance (r_S) is the main limiting factor to achieve a high performance for a multi-junction solar cell working under hundreds of suns concentration. Due to the complex constituent elements of series resistance, several aspects of the design and manufacture of the solar cells must be considered carefully. The gridline geometries and the metal structure of the triple junction solar cell are the most important factors to reduce the r_S . The main concerns are as follows: What is the best r_S value? Which steps during the whole manufacture process will affect the r_S value mostly?

It is known that there are many constituent elements contributed to the series resistance,

$$r_S = r_L + r_V + r_G + r_{FC} + r_{BC} \tag{22}$$

$$\frac{1}{r_L} = \frac{1}{r_E} + \frac{1}{r_W} \tag{23}$$

$$r_V = r_B + r_{Su} \tag{24}$$

where r_L is the resistance of the lateral current in the semiconductor structure, r_V is the resistance of the vertical current, r_G is the contribution of gridline, r_{BC} is the resistance of other symbols, and r_{FC} is resistance of the front contact. r_E and r_W are the contribution of emitter layer and window layer to the r_{El} espectively. r_B and r_{Su} are the contribution of base layer and substrate to the r_V respectively.

Traditionally the front metal grid of concentrator solar cells has been thickened up to 5~7 micrometers by electroplating. The higher ratio of the thickness to the width of the grid lines results in larger profile area. On the other hand, the resistance of the gridline metal (r_G) affects the series resistance of the solar cells greatly.

Due to the low thickness (100~150 nm) of the contact semiconductor layer, the lateral resistance in the semiconductor (r_L) also plays an important role in the constituent elements of series resistance. An effective method to reduce the r_L , is to decrease the space between the

http://dx.doi.org/10.5772/50965

neighbour gridlines, which can be described as the shadowing factor, Fs: a ratio of Area covered by metal to total area. As the shadowing factor increases, the area of the front contact will increase and the series resistance components related to the front contact, r_{FC} , decreases. The lateral current can be easier to collect through a shorter distance. Unfortunately, the shadow of the front grid line increases as the shadowing factor increasing, resulting in a reduction of the Isc of the solar cell. Therefore, the balance between the lower lateral resistance and higher Isc related to the shadowing factor should be considered carefully.

Experimental verification is carried out to obtain the optimum front grid design for 1000 suns concentration GaInP/GaInAs/Ge multi-junction solar cells. Typical values of the front contact resistance (r_{FC}) and the thickness of the grid line metal are 5×10^{-5} Ω.cm^2 and 7 micrometers, respectively. The front contact metal sheet resistance, r_{Msheet} , ranges from 3 to 5×10^{-6} Ω.cm^2. The space between the neighbour gridlines are in the range of 45 ~167 micrometers, respectively. All the Fs and WL values are referred to fingers of 7 micrometers thick in a 10×10 mm2 sized solar cell. It must be pointed that there is no antireflection coating on the surface of all the solar cells discussed here.

Figure12 (a) shows the short-circuit current (Isc), fill factor (FF) and efficiency (Eff) as a function of the shadowing factor. It is evident that with the wider space, the higher Isc can be obtained, because more light can be absorbed by the solar cell. The FF increases obviously as the space increases. Therefore, we can draw a conclusion that the optimal front gridline design should result in higher Isc and FF. As shown in Figure 12 (b), the highest Isc×FF is found with an Fs of 5%, and the corresponding efficiency of 29.8% is also the highest one.

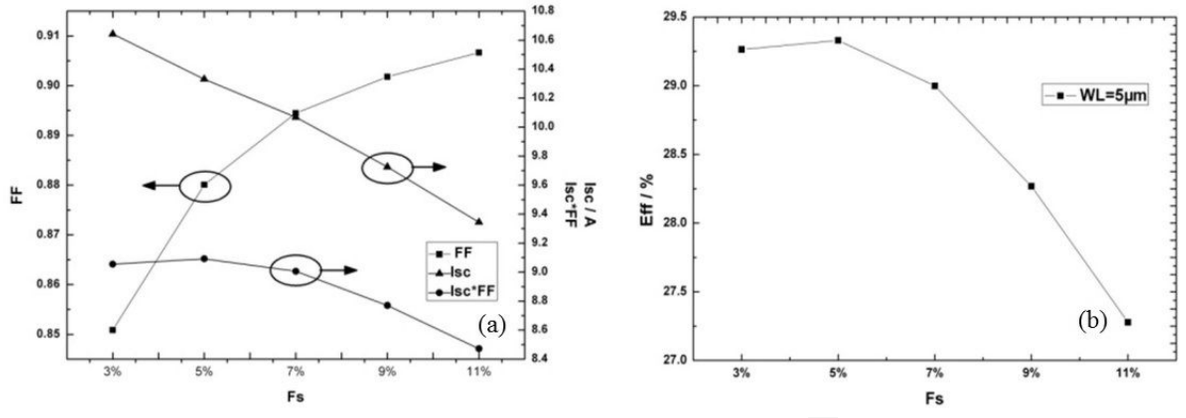

Figure 12. The short-circuit current (Isc), fill factor (FF) and efficiency (Eff) as a function of the shadowing factor.

3.2.2.2. Antireflection Coating

Due to the high refractive indices of semiconductors, high reflection losses must be minimized by antireflection coatings (ARC) for GaInP/GaInAs/Ge multi-junction solar cells. This presents several challenges for the ARC design. Firstly, the wide wavelength range of sunlight requires an optimization of extreme broadband design and limits the material choice to

those with little or no absorption over the required wavelength range. For high concentrator multi-junction solar cells, the direct terrestrial sunlight spectrum (AM1.5D), defined for a zenith angle of 48.2° representing the average conditions of the United States, is split between each sub-cell in this triple junction design as shown in Figure13. The bandwidth of absorption and internal quantum efficiency extends in both the UV and IR directions, ranging from 300~1800 nm. Secondly, for the concentrator multi-junction solar cells, light is incident upon the cell over a wide angular range, introducing an additional dimension for optimization. Thirdly, solar cells are required to operate for 20~30 years. Materials must not be modified or damaged by long-term exposure to UV light or large periodic changes in temperature and humidity. Furthermore, variations in the temperature-dependence of the refractive index of each layer will lead to a temperature-dependent transmission spectrum which may affect the performance of multi-junction solar cells. Finally, these ARC layers should be deposited inexpensively over large areas, together in a single coating chamber, and at low temperatures to minimize impact on the solar cell performance.

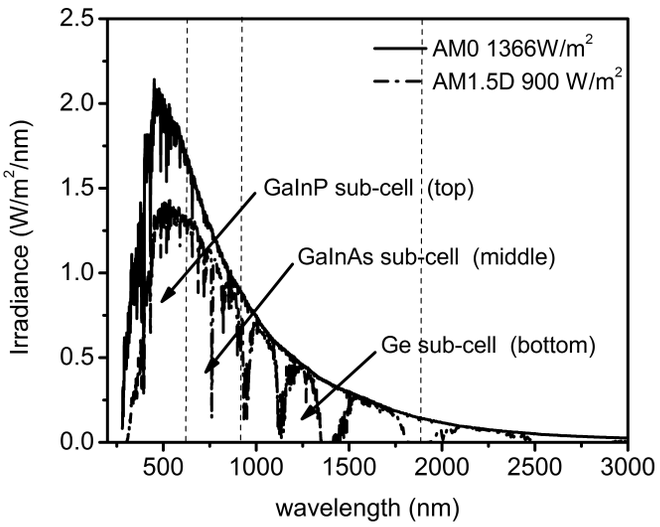

Figure 13. The wavelength versus irradiance spectrum.

In the triple junction solar cells, the window layer of the top cell, AlInP, was considered for the ARC designs, using a structure (air, ARC layer(s), AlInP) with direct normal incidence AM1.5D sunlight. Figure14 shows the reflection spectra for two-layer material combinations commonly used for antireflection coatings. Both Al_2O_3/TiO_2 and SiO_2/TiO_2 offer coating solutions using practical deposition equipment. Commercially deposited Al_2O_3/TiO_2 coatings have shown a 30-35% improvement in the Isc and a corresponding smaller increase to Voc when compared with uncoated devices.

Figs.15 shows the improvement in the external quantum efficiency (EQE) of the cells with Al_2O_3/TiO_2 coatings. It can be seen that an improvement in the EQE (AM1.5D) of the top and middle cells is from 65% to 88%. Figure16 shows the improvement in the optical and electri-

http://dx.doi.org/10.5772/50965

cal properties of the samples above. It can be seen that the Isc under 1000 suns is improved from 10.27 to 13.79 A, and the improvement in the Isc is 34.3%; the Voc also has a small increase of 0.03V. The FF shows an obvious decrease of 1.9% because of more ohmic loss with higher Isc. The efficiency of the samples with Al_2O_3/TiO_2 coatings combination increases from 29.33% to 39.30%, a 34.0% improvement.

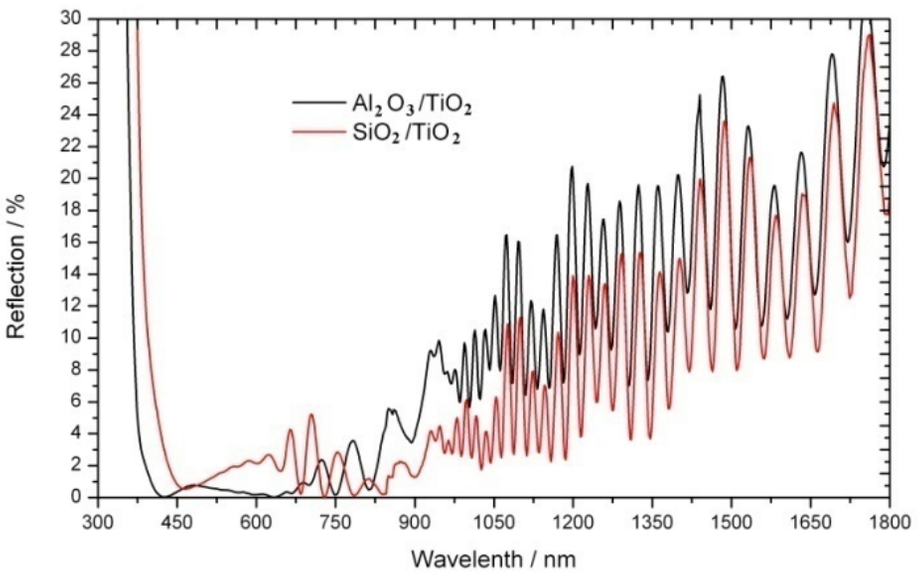

Figure 14. The reflection spectra of the solar cells with ARC.

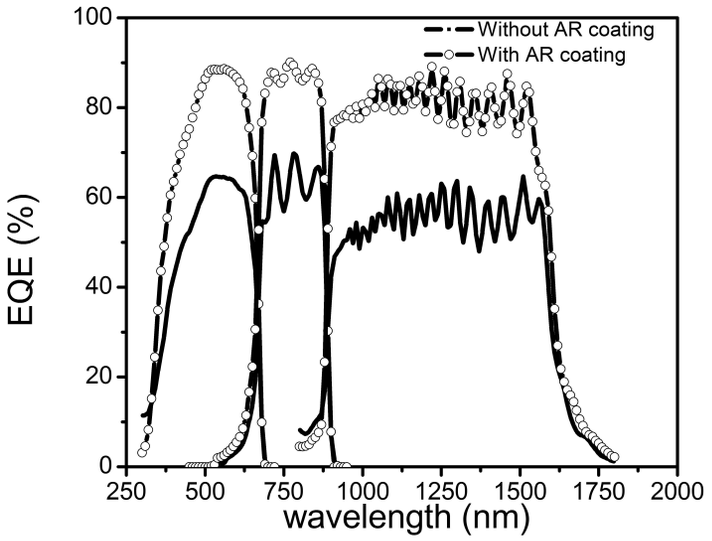

Figure 15. The EQE of the cells with and without ARC.

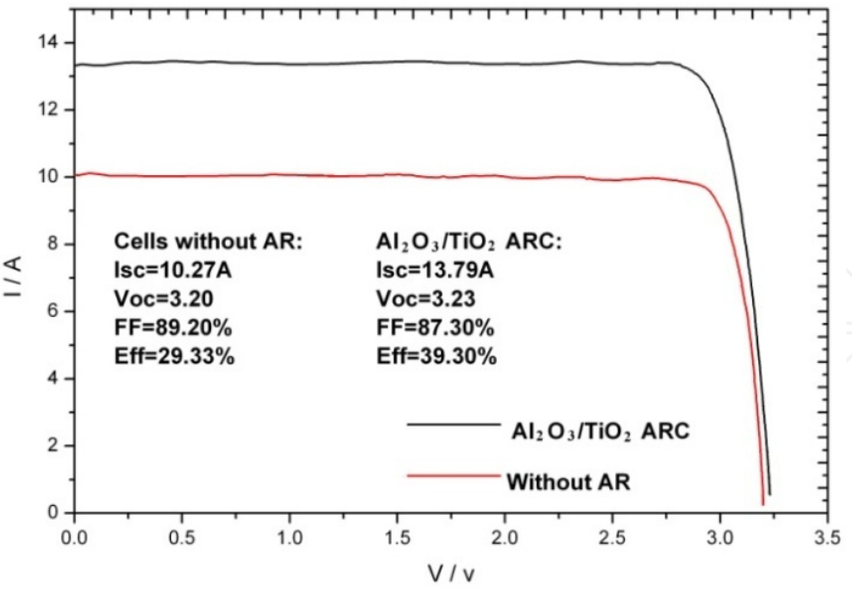

Figure 16. The optical and electrical properties of the cells with and without ARC.

4. The reliability of the multi-junction solar cell

4.1. Accelerated aging tests

Under high concentration of several hundreds or even thousands suns, multi-junction solar cells will suffer high temperature and high current density, which are challenging the reliability of these devices [16]. To obtain the approval from CPV customers, it is necessary to demonstrate the reliability of multi-junction solar cells operating under high concentration.

A new certification standard, namely the IEC62108, has been developed in which the procedure for qualifying CPV systems and assemblies is described. The IEC62108 is currently the only international standard on assessment of high concentration solar receivers and modules, which specifies the minimum requirements for the design qualification and the type approval of concentrator solar cells, and which gives the corresponding test procedures for each test sample, such as outdoor exposure test, electrical performance measurement, electrical test, irradiation test, and mechanical load test. After passing the IEC62108 certification, both the modules and assemblies can be suitable for long-term (25 years) operation in general open-air climates.

The purpose of the thermal cycling test is to determine the ability of the receivers to withstand thermal mismatch, fatigue, and other stresses caused by rapid, non-uniform or repeated changes of temperature. This test is vital to the reliability of concentrator solar cells, since generally these devices have to operate at high concentration of more than 1000 suns, high operation current density of more than 10A/cm^2, high operation temperature of more than 60 °C and large temperature difference between day and night.

http://dx.doi.org/10.5772/50965

In order to simulate the real operating conditions, IEC 62108 requires that during the process of thermal cycling test for concentrator solar cells carried out in the oven, a current should be flowing through the chips. Table 6 shows the three optional conditions. In principle, the temperature and the current injection time of cells are required to be accurately monitored during thermal cycling test. However, it is very difficult to monitor the real temperature of cells in real operating conditions, because a high electric current passing through the cells can lead to differences in temperature among the cells, the heat sink and the oven.

Option	Maximum cell temperature	Total cycles	Applied current
TCA-1	85 °C	1000	Apply 1.25×Isc when T "/ 25°C , cycle speed is 10 electrical/thermal
TCA-2	110 °C	500	Apply 1.25×Isc when T "/ 25°C , cycle speed is 10 electrical/thermal
TCA-3	65 °C	2000	Apply 1.25×Isc when T "/ 25°C , cycle speed is 10 electrical/thermal

Table 6. The options of thermal cycling test from IEC 62108.

Using the thermal cycling test condition of TCA-1 from table 6, the cell temperature is controlled between -40 °C and 85 °C. A dwell time of 10 min of the high and low temperatures is required. The cycling period and frequency are 120 minutes and 12 cycles per day, respectively. In one thermal cycle, a specific current level of 7A is periodically on and off for 10 cycles, when the cell temperature is above 25 °C. In order to illustrate the changes of electrical performance of test samples, control samples are chosen and measured under the similar test condition. By this method, test condition variables are self-corrected, and the complex translation procedures are eliminated. Finally, the relative power Pr and relative power degradation Prd are defined as follows:

$$P_r = \frac{P_m}{P_{mc}} \times 100\% \tag{25}$$

$$P_{rd} = \frac{P_{ri} - P_{rf}}{P_{ri}} \times 100\% \tag{26}$$

where Pm is the test sample's maximum power, Pmc is the control sample's maximum power measured at the similar condition as Pm, and Prf and Pri are the relative powers measured after and before the given test, respectively.

For comparison, eight San'an company's cells and eight B-company's cells were tested together. Tables 7 and 8 show the relative power degradation of San'an Company's and B-company's receiver samples after different numbers of thermal cycles, respectively. The

output powers gradually decrease with the increasing thermal cycles due to the samples' degradation. It is found that the relative power degradations of tested samples are within 10%. The degradation is believed to be responsible for the perimeter degradation [16, 17]. According to González et al., the arbitrary definition of device failure is a 10% of power loss, so the majority of test samples do not have failure, except the c B-company's receiver #56, the relative power degradation of which is from 12.85% after 560 thermal cycles to 14.89% after 1000 thermal cycles. Besides, from visual inspection on these samples, the DBCs soldered on alumina substrates are not peeled off after the 1000 thermal cycles, which indicates that it is suitable for long-term (~25 years) operation in general open-air climates.

Serial sample	0 cycle	360 cycles	560 cycles	760 cycles	1000 cycles
#182B5	0.00%	-2.47%	-4.00%	-5.56%	-8.02%
#183D1	0.00%	-0.14%	-3.19%	-3.88%	-5.44%
#182D5	0.00%	-3.66%	-4.78%	-5.82%	-8.21%
#183B1	0.00%	-2.48%	-4.83%	-6.33%	-8.25%
#182D1	0.00%	-4.62%	-5.38%	-6.21%	-7.95%
#183B6	0.00%	-5.85%	-6.08%	-5.84%	-7.09%
#183A4	0.00%	-5.02%	-5.70%	-6.97%	-7.96%
#183D5	0.00%	-5.47%	-5.83%	-6.06%	-7.37%

Table 7. Relative power degradation of San'an Company's receiver samples after different numbers of thermal cycles.

Serial sample	0cycle	360cycles	560 cycles	760 cycles	1000 cycles
#112	0.00%	-5.93%	-6.83%	-6.84%	-7.72%
#44	0.00%	-4.10%	-5.60%	-6.12%	-8.11%
#56	0.00%	-8.02%	-12.85%	-13.05%	-14.89%
#94	0.00%	-2.76%	-4.94%	-5.19%	-6.78%
#78	0.00%	-5.17%	-6.39%	-6.76%	-7.36%
#90	0.00%	-7.14%	-7.75%	-8.17%	-8.32%
#97	0.00%	-3.19%	-3.38%	-4.38%	-7.42%
#136	0.00%	-6.30%	-6.69%	-7.05%	-9.34%

Table 8. Relative power degradation of B-company's receiver samples with different numbers of thermal cycles.

In conclusion, high concentration multi-junction solar cells are still at an early stage of technological development, and thus it is necessary to demonstrate the reliability of these solar cells before their industrialization. Accelerated aging test is a necessary tool to demonstrate the reliability of concentration photovoltaic solar cells, which is expected to be working for

no less than 25 years. According to the requirements from IEC 62108, this paper presents the reliability results from thermal cycling tests performed on San'an company's high concentration solar cells. We find that the light emitting intensity and the relative power degradation of San'an company's receivers are similar to that of B-company's receivers.

4.2. Discussion on outdoor power plant performance

Concentrated photovoltaic (CPV) system is usually located in sunny places for large-scale photovoltaic (PV) power station with installation capacity of 1~1000 megawatt (MW). It is composed of Fresnel lenses to concentrate, III-V multi-junction solar cells, polar axis type or pedestal type tracking system and integrated control method. By focusing sunlight onto high-efficiency solar cells, CPV is able to use fewer solar cells than traditional photovoltaic power. Since CPV has a high power-generating capacity with movable parts, easy to manufacture and to maintain, it is very suitable for a large scale PV power station.

According to the CPV Consortium, "CPV, with its higher efficiency delivers higher energy production per megawatt installed, provides the lowest cost of solar energy in high solar regions of the world. The technology is in its early stage with significant headroom for future innovation, and it has the ability to ramp to gigawatts of production very rapidly. Many of the limitations for PV in the past are overcome by advances in CPV technology."As of 2011, the global bases of installed CPV produced totally just 60 megawatts, according to the CPV Consortium. The organization predicts that capacity will rise to 275 megawatts by the end of 2012, 650 megawatts by the end of 2013, 1,100 megawatts by end of 2014 and 1,500 megawatts by the end of 2015.

World-widely, 40 MW Amonix power plants will be installed from 2012 on, at the same time 32.7 MW power plant located at Alamosa Colorado was measured during the week of March 2012. ISFOC (Institute of Concentration Photovoltaic Systems) main goal is to promote the CPV industrialization. For this purpose, ISFOC has made the installation of CPV Plants, up to 2.7 MW, all over the region of Castilla la Mancha. A lot of CPV power plants will be installed in near future without being introduced more. However, focusing on China, the relative long history of advanced CPV technology development, the years' experience of power plant operation, mature systems with high performance and reliability, the leading position of the western participants will set up a benchmark in the field and gain more attention and more shares from Chinese CPV market. For a few domestic CPV companies with installation records, further efforts are required to improve the performance and reliability of CPV products, to lower the cost by setting up complete supply chains in CPV industry, to facilitate the utilization of abundant solar resources from the north and west to the south and east via setting up transmission networks, so that a Chinese CPV market can be actually initiated, developed and matured.

The largest CPV power plant project in China was assembled at Golmud, Qinghai province by Suncore Photovoltaic Technology Co., Ltd, with the capacity of more than 50 MW. Suncore is a Sino-US joint venture established by San'an and Emcore. 1 MW of the project using 500 suns terrestrial system and 2MW using 1000 suns terrestrial system has been finished, as

shown in Figure 17. Conversion efficiency of 500 suns and 1000 suns terrestrial system can reach as high as 25% and 28.5%, respectively.

Figure 17. power plant installed at Golmud Qinghai province China.

The direct normal insolation (DNI) distribution of the local environment and the mapping of China were displayed Figure 18 (a) and (b). The I-V curves of 227 receivers using 500 suns terrestrial system module tested outdoor was shown in Figure 19. One can see that the efficiency could reach as high as 24.03% at the condition of much dust on the surface of the Fresnel lens, which affecting the light transmittance. Therefore, the actual efficiency should be high than this nominal value.

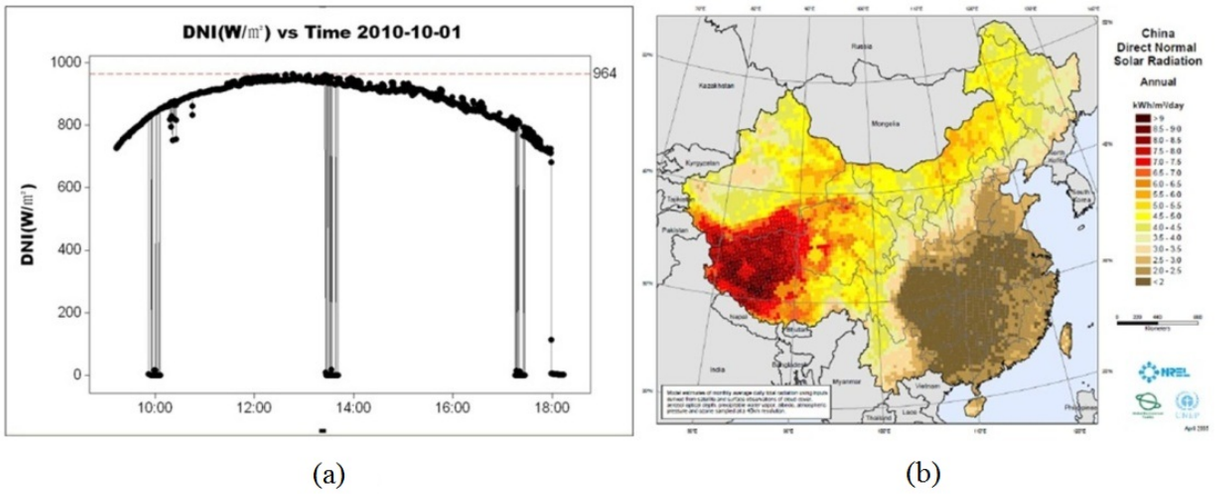

Figure 18. The DNI distribution of the whole day in Golmud (a), and the annual average direct normal insolation (DNI) GIS data at 40km resolution for China (b) from NREL.

http://dx.doi.org/10.5772/50965

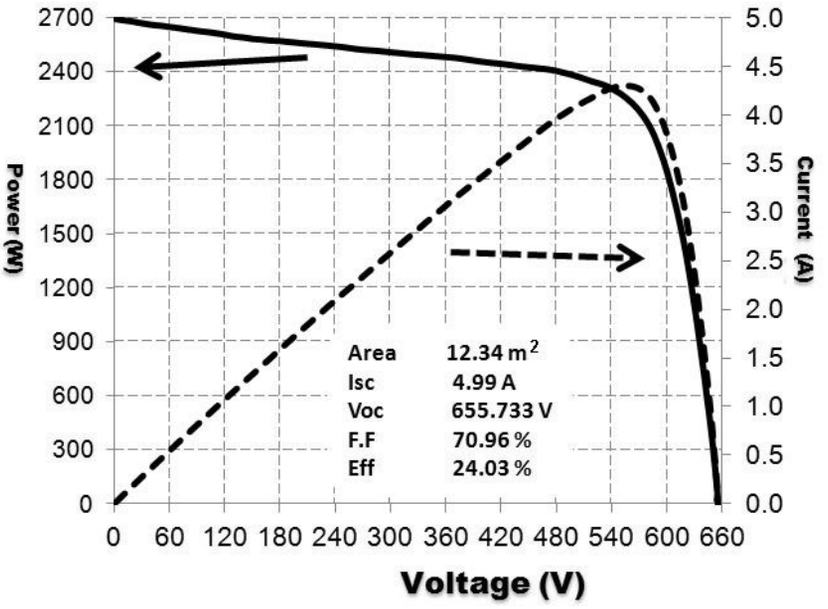

Figure 19. I-V curves of the 227 Receivers module tested outdoor.

Acknowledgements

This work was supported by a foundation from the National High Technology Research and Development Program (863 program) of China. (No. 2012AA051402).

Author details

Gui jiang Lin[1], Jingfeng Bi[1], Minghui Song[1], Jianqing Liu[1], Weiping Xiong[1] and Meichun Huang[2*]

*Address all correspondence to: mchuang@xmu.edu.cn

1 Xiamen San'an Optoelectronics Co., Ltd., China

2 Department of Physics, Xiamen University, China

References

[1] Green, M. A. (2005). *Third generation photovoltics*, Berlin, Springer.

[2] Luque, A., Martı´, A., Stanley, C., Lo´pez, N., Cuadra, L., Zhou, D., & Mc Kee, A. (2004). General equivalent circuit for intermediate band devices: Potentials, currents and electroluminescence. *J. Appl. Phys.*, 96(03), 903-909.

[3] King, R. R. (2008). Multi-junction solar cells: Record breakers. *Nature Photonics*, 2, 284-286.

[4] King, R. R., Law, D. C., Edmondson, K. M., Fetzer, C. M., Kinsey, G. S., Yoon, H., Sherif, R. A., & Karam, N. H. (2007). 40% efficient metamorphic GaInP/GaInAs/Ge multi-junction solar cells. *Appl. Phys. Lett.*, 90(18), 3516-3518.

[5] Yamaguchi, M., Takamoto, T., & Araki, K. (2006). Super high-efficiency multi-junction and concentrator solar cells. *Sol. Energy Mater. Sol. Cells*, 90-3068.

[6] Daniel, C. L., King, R. R., Yoon, H. M., Archer, J., Boca, A., Fetzer, C. M., Mesropian, S., Isshiki, T., Haddad, M., Edmondson, K. M., Bhusari, D., Yen, J., Sherif, R. A., Atwater, H. A., & Karama, N. H. (2010). Future technology pathways of terrestrial III-V multi-junction solar cells for concentrator photovoltaic systems. *Solar Energy Materials & Solar Cells*, 94, 1314-1318.

[7] Geisz, J. F., Kurtz, S., Wanlass, M. W., Ward, J. S., Duda, A., Friedman, D. J., Olson, J. M., Mc Mahon, W. E., Moriarty, T. E., & Kiehl, J. T. (2007). High-efficiency GaInP/GaAs/InGaAs triple-junction solar cells grown inverted with a metamorphic bottom junction. *Appl. Phys. Lett.*, 91(02), 3502-3504.

[8] Guter, W., Schöne, J., Philipps, S. P., Steiner, M., Siefer, G., Wekkeli, A., Welser, E., Oliva, E., Bett, A. W., & Dimroth, F. (2009). Current-matched triple-junction solar cell reaching 41.1% conversion efficiency under concentrated sunlight. *Appl. Phys. Lett.*, 94(22), 3504-3506.

[9] Fahrenbruch, A. L., & Bube, R. H. (1983). *Fundamentals of Solar Cells Photovoltaic Solar Energy Conversion*, New York, Academic Press.

[10] Würfel, P. (2005). *Physics of solar cells: From principles to new concepts. Verlag GmbH & Co KGaA*, Weinheim, Wiley-VCH.

[11] Olson, J. M., Ahrenkiel, R. K., Dunlavy, D. J., Keyes, B., & Kibbler, A. E. (1989). Ultralow recombination velocity at Ga0.5In0.5P/GaAs heterointerfaces. *Appl. Phys. Lett.*, 55, 1208-1210.

[12] Palik, E. D. (1991). *Handbook of Optical Constants of Soilds II*, San Diego, USA, Academic Press.

[13] Kalyuzhnyy, N. A., Gudovskikh, A. S., Evstropov, V. V., Lantratov, V. M., Mintairov, S. A., Timoshina, K. H., Shvarts, M. Z., & Andreev, V. M. (2010). Germanium Subcells for Multi-junction GaInP/GaInAs/Ge Solar Cells. *Semiconductors*, 44(11), 1520-1528.

[14] Ebert, C., Pulwin, Z., Byrnes, D., Paranjpe, A., & Zhang, W. (2010). Tellurium doping of InGaP for tunnel junction applications in triple junction solar cells. *Journal of Crystal Growth*, 315, 61-63.

[15] Garcia, I., Rey-Stolle, I., Algora, C., Stolz, W., & Volz, K. (2008). Influence of GaInP ordering on the electronic quality of concentrator solar cells. *Journal of Crystal Growth*, 310, 5209-5213.

[16] González, J. R., Vázquez, M., Núñez, N., Algora, C., Rey-Stolle, I., & Galiana, B. (2009). Reliability analysis of temperature step-stress tests on III-V high concentration solar cells. *MICROELECTRONICS RELIABILIBTY*, 49, 673-680.

[17] Algora, C. (2010). Reliability of III-V concentrator solar cells. *MICROELECTRONICS RELIABILIBTY*, 50, 1193-1198.

IntechOpen